CHAPTER 4

Highly facile Ag/NiO nanocomposite synthesized by sol-gel method for mineralization of rhodamine B

4.1 Introduction

The discharge of certain industrial effluents from the paint, drugs, food, textiles, leather, and many other industries with various toxic substances to the aquatic environment has necessitated the importance of monitoring, control, and removal of these toxic species because of their non-biodegradable nature, they impose various diseases to the whole biota. Hence, the elimination of organic effluents' is vital for making a safe and healthy environment (Fox and Dulay, 1993). Over the past few decades, photocatalysis gained much popularity, particularly in solving energy and pollution problems, whose precise intention is to provide an economical and environment-friendly catalyst along with sufficient capacity for mineralization (Fujishima and Honda, 1972). The band gaps of the individual semiconductors generally do not allow the mineralization process, resulting to which their application become relatively narrower. Therefore, it is required to develop new kinds of photocatalysts with high activity in the presence of sunlight by modifying the semiconductors. From the last several decades, vast varieties of the metal oxides like TiO_2, ZnO, Fe_2O_3, NiO, AgO, and Co_3O_4 have been used for the mineralization of hazardous pollutants photochemically. However, all these photocatalysts harbor certain limitations like (i) less transmittance of light, (ii) aggregation of the nanoparticles, and (iii) lower surface area. Thus further innovation is required in the design and synthesis of the suitable combinations of the materials in order to enhance the photocatalytic efficiency. El- Kemary et al. plead nickel oxide has good catalytic activity because of their super durability, strong photosensitivity as well as its high absorptivity affinity (El-Kemary et al., 2013). The scope of NiO nanoparticles' is very vast, including storage battery, sensor, magnetic material, and catalysis (Ramesan and Santhi, 2017; Alagiri et al., 2012; Wu et al., 2007; Xin et al., 2007).

However, pure NiO nanoparticles have very few applications because of the poor defects, i.e., less oxygen vacancy or interstitial nickel resulting in poor optical properties (Sabouri et al., 2019). So, the solution to this problem is doping, i.e., insertion of impurities into semiconductors, which modify the properties of the raw materials (Ghazal et al., 2020). Of late, doping of gold, silver, palladium, and platinum has attracted more attention because of their potent mineralization of organic pollutants. Loading of the noble metals on the semiconductors surfaces facilitate them to absorb spectrum of the visible region because they lowers the band gaps of the semiconductors and forms a strong electromagnetic field through the Localized Surface Plasmon Resonance (LSPR) as well (Bai et al., 2014; Sun et al., 2009; Kale et al., 2014). Silver has been preferred to other noble metals because it shows good LSPR phenomenon (Wang et al., 2008). In recent years, nanocomposite Ag/NiO was prepared using various methods for different applications in sensors, energy storage, and many others (Ashok Kumar Reddy et al., 2014; Yang et al., 2013; Wu et al., 2017; Song et al., 2013; Ding et al., 2010). To date, only one reports of Ag/NiO is published in the field of photocatalysis, mainly for the mineralization of RhB dye (Ghazal et al., 2020). In the current study, we report the photocatalytic performance of the Ag/NiO nanocomposite photocatalyst on rhodamine B (RhB) dye under ultraviolet light, which was synthesized by adapting a sol-gel route (Alagiri et al., 2012). Our synthesized heterostructured nanocomposites have higher photocatalytic degradation efficiency, linear coefficient (R^2) as well as higher rate constant and TOF value than previous work on Ag/NiO (Ghazal et al., 2020). As prepared nanocomposite photocatalyst controls electron/hole recombination resulting in charge separation between excitons, and it also provides a large surface area and interface to create oxygen vacancies, which is efficient to make it a superior candidate for the mineralization

process.

4.2 Experimental

4.2.1 Synthesis of NiO

NiO (L-1) was synthesized by the sol-gel route by using $Ni(NO_3)_2 \cdot 6H_2O$ as a precursor. $Ni(NO_3)_2.6H_2O$ and anhydrous citric acid in 1:1 M ratio were dissolved in 50 mL deionized water by maintaining the pH at 1. The mixed solution was stirred at 70 °C for 16 h. The viscous sample was then dried at 105 °C in a hot air oven; the dried sample was crushed properly in a pestle-mortar and further calcined at 400 °C for 4 h in a muffle furnace.

4.2.2 Synthesis protocol of Ag/NiO heterostructure

100 mg of as-synthesized NiO (L-1) was dispersed in 50 mL of water to which 6 mg of $AgNO_3$ was added. This was further reduced with 15 mL of 0.02M $NaBH_4$ with continuous stirring for 4 h. The resulting sample was centrifuged and washed several time, and dried in an oven. Different loading percentage of photocatalyst Ag/NiO was prepared by similar route only by varying the amount of silver nitrate. Hereafter in this chapter 4, 6, and 8 wt% of $AgNO_3$ in Ag/NiO samples will be referred to as LT-1, LT-2, and LT-3, respectively. The whole process is summarized in figure 4.1. Furthermore, similar synthetic protocol was followed for the synthesis of Ag nanoparticles (T-1) bereft of NiO, which was used as a control.

4.3 Characterization

All the samples were characterized by different techniques discussed in chapter 2.

4.3.1 Photocatalytic efficiency

The photocatalytic mineralization process of the RhB dye was examined under UV light (254 nm, Phillips, 8W) over different photocatalyst. 0.01 mg of synthesized samples was dispersed

separately in a 100 mL aqueous solution of RhB (10 ppm) dye and the reaction mixture was irradiated with the UV light. A pictorial of photocatalytic chamber is given in figure 4.2. Complete reactions were performed in a quartz cuvette of 1 cm path length and analyzed by the UV–Vis. spectrophotometer. Variation in the absorbance of the dye with respect to time indicates the mineralization process. The percentage of RhB degradation was investigated by using equation (3.1).

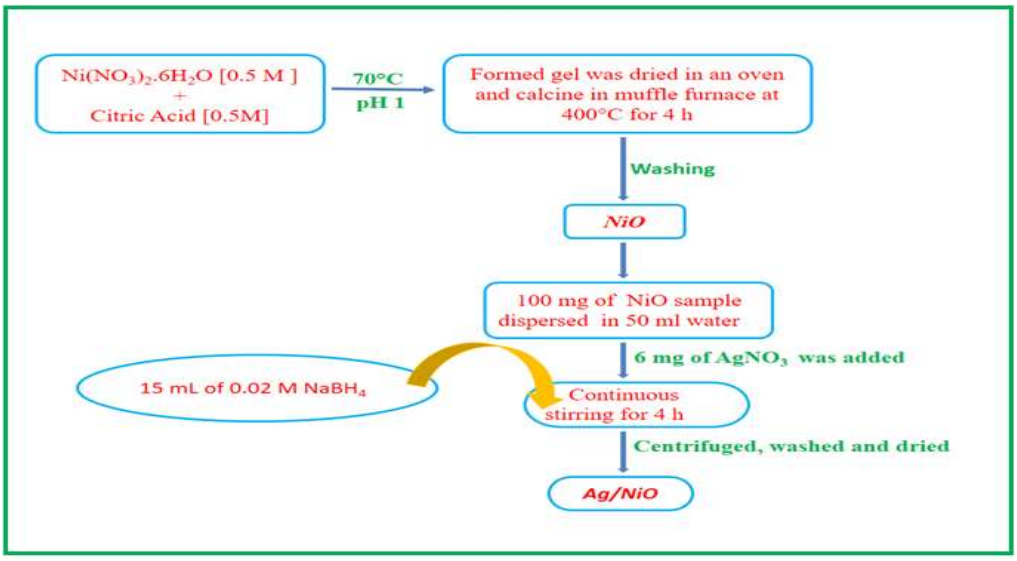

Fig. 4.1 Schematic representation for the synthesis of Ag/NiO

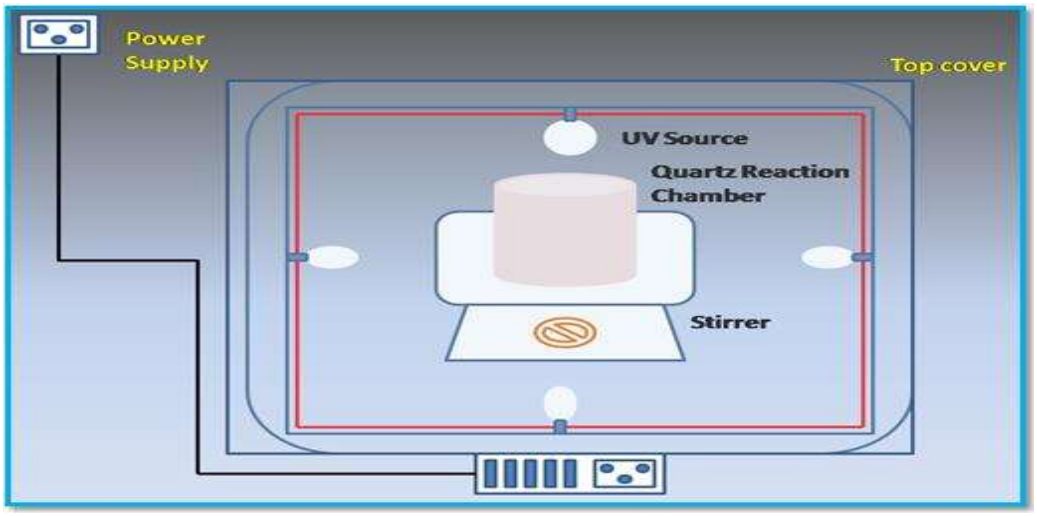

Fig. 4.2 Photocatalytic reaction chamber

4.4 Result and discussion

4.4.1 HR-XRD

The crystal structure and purity of the prepared photocatalysts were analyzed by HR-XRD. Figure 4.3a depicts the XRD pattern of the samples L-1, LT-1, LT-2, LT-3, and T-1 was characterized by the conventional method for obtaining their structural information and phases. For T-1 sample, which is Ag nanoparticle, four peaks were observed at 2θ values 37.9°, 43.9°, 64.3°, and 77.2°, which are assigned to [111], [200], [220], and [311] respectively (JCPDS card no. 87–0719) depicts the cubic structure of Ag. In case of NiO (L-1) fine peaks at 2θ values 37.2°, 43.3°, 62.9°, 75.4°, and 79.4° are obtained, which are indexed at [111], [200], [220], [311], and [222] planes respectively (JCPDS card no. 47–1049), indicates the cubic phase of NiO nanoparticles. All the characteristic peaks of both the Ag and NiO appeared in the LT-1, LT-2 and LT-3 samples, which confirm the presence of Ag along with NiO nanoparticles without any additional peaks. The obtained results are in good agreement with the findings of Lin-Xia Zhou et al. 2020 and sadayappan Nagamuthu et al. 2019 (Zhou et al., 2021; Nagamuthu and Ryu, 2019).

4.4.2 FT-IR Analysis

To know the vibrational behavior and functional group of the molecule, we recorded the FT-IR spectrum of synthesized samples, results of which are displayed in figure 4.3b. According to the results of FT-IR spectrum, the band range from 3200-3500 cm^{-1} corresponds to the O-H vibrational stretching mode, which is due to the moisture absorbed from the atmosphere. Another band recorded at 1630 cm^{-1} in sample L-1 and 1632 cm^{-1} in sample LT-2 is related to the bending vibration of water molecule (Baig et al., 2020) . A band at 426 cm^{-1} is recorded for sample L-1, which occurs because of the Ni-O stretching vibration (Selvarajan

et al., 2018). All vibrational modes of sample L-1 are also recorded into the spectrum of LT-2 sample with slight variation in wavenumber of the band along with them some different bands, i.e., 1090 and 1383 cm^{-1} are assigned to symmetric and asymmetric vibrational modes of the CO_2, respectively (Alrebdi et al., 2022; Aydoghmish et al., 2019). These vibrational modes are mainly come out from the adsorbed atmospheric CO_2 or ethanol (El-Kemary et al., 2013). The intensity of these bands is weak, which confirms that the adsorption modes are physical. From the above observation, we conclude that the formation of NiO takes place. In spectrum, no other vibration modes are obtained; it means that our synthesized sample is highly pure without any secondary phase.

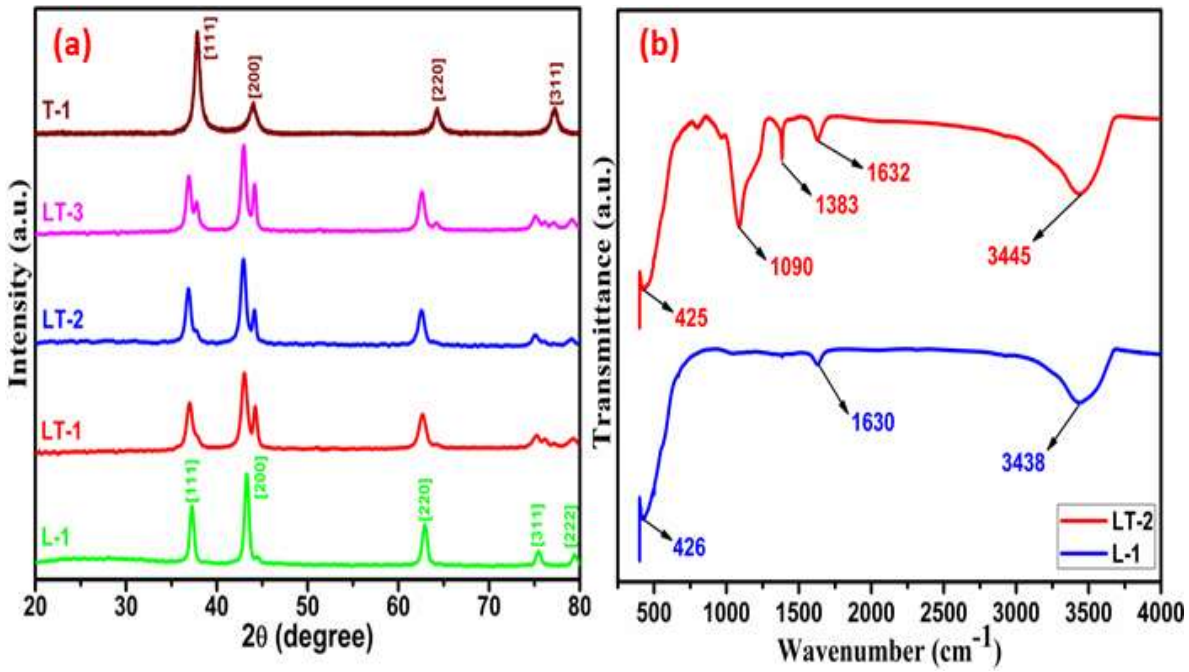

Fig. 4.3 (a) HR-XRD pattern of L-1, LT-1, LT-2, LT-3 and T-1, (b) FT-IR of L-1 and LT-2

4.4.3 Morphology measurements (TEM and FE-SEM)

The morphological and particle size analysis was performed to characterize all samples with TEM and FE-SEM micrographs depicted in figures 4.4 and 4.5 respectively. TEM micrograph of LT-2 is shown in figure 4.4a, which confirms the homogenous mixing of

nanoparticles and their spherical morphology, SAED pattern of LT-2 (inset of figure 4.4a) ratifies the polycrystalline nature of LT-2 nanocomposite. Figure 4.4b shows the histogram of the average particle size of LT-2, and it was in the range of 15–20 nm.

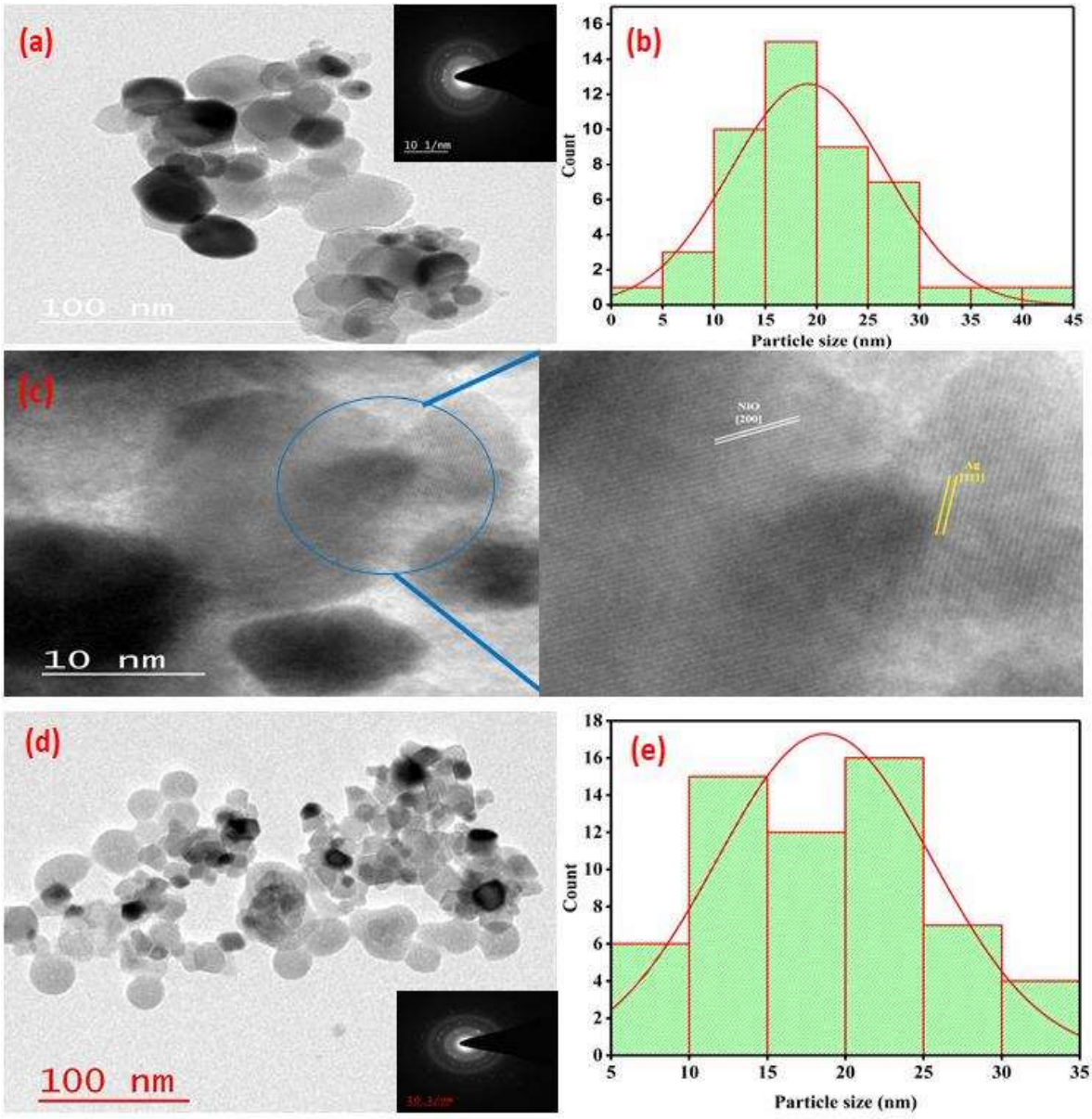

Fig. 4.4 (a) TEM image of LT-2 and SAED pattern of LT-2 (inset), (b) Histogram of average particle size of LT-2, (c) HR-TEM of LT-2, (d) TEM micrograph and SAED pattern (inset) of L-1, (e) Histogram of L-1 displaying average particle size

Figure 4.4c displays the HR-TEM image of LT-2, which reveals that there is close interfacial contact in between Ag and NiO particles. The d spacing value of the fringes was calculated and found corresponding to the [111] and [200] lattice planes of Ag and NiO, respectively. The particles of pure NiO (L-1) are also slightly spherical in shape with an average size of 18 nm (figure 4.4d and e). The TEM and XRD results (crystallite size, crystallinity, crystal structure etc.) of the nanocomposite are in good agreement with each other; these results along with HR-TEM confirm the loading of Ag with NiO nanoparticles (NPs). Further the FE-SEM and EDX measurement were carried out to explore the surface morphology and distribution of Ag over the surface of NiO. Figure 4.5a and b displays the FE-SEM micrographs of the bare and Ag/NiO (LT-2) nanoparticles, respectively. As figure 4.5a and b clearly shows the porous honeycomb-like morphology of NiO surfaces and loading of Ag does not significantly change the morphology of the NiO, and Ag appears in the pores of NiO. Figure 4.5c and d shows the results of the EDS measurement of the pure and Ag loaded NiO NPs. Figure 4.5d confirms the existence of Ag into the modified NiO nanoparticle along with the basic constituents Ni and O. The presence of the distinct signals correspond to these elements is strong evidence for the presence of Ag over the surface of NiO host structure.

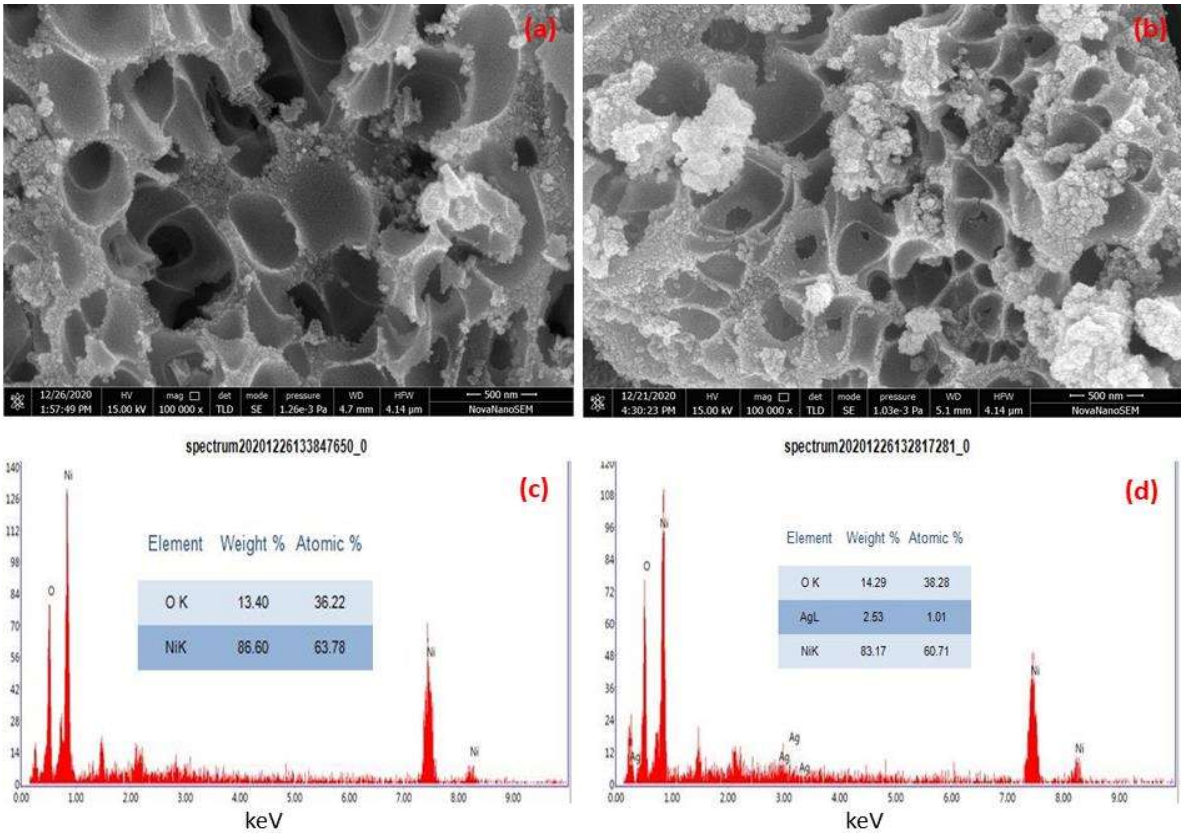

Fig. 4.5 (a, b) FE-SEM image of L-1 and LT-2 respectively, (c, d) EDS of L-1 and LT-2 respectively

4.4.4 X-ray photoelectron spectroscopy (XPS) analysis

XPS measurement helps to examine the elements and their chemical state present in the sample. We performed XPS analysis for LT-2 photocatalysts, the results of which is given in figure 4.6. The Synthesized heterostructure contains O (photoelectrons from 1s), Ag (3d), and Ni (2p) elements only; means our synthesized catalysts are free from impurities. The core-level spectrum of the Ag (3d) is shown in figure 4.6a. Two prominent peaks at 368.30 and 374.20 eV were observed, which attribute to Ag $3d_{5/2}$ and Ag $3d_{3/2}$, respectively. The observed peaks and splitting of the 3d into doublet signal confirms the existence of metallic Ag, which is in good agreement with the previously reported results (Ngo et al., 2017; Chen

et al., 2011). Doublet peaks of Ag 3d may be due to the splitting occurs during the exchange interaction between the unpaired valence electrons and the unpaired electron left in the core level (after photoionization) In figure 4.6b, peaks at 529.27 and 530.71 eV are the peaks of oxygen that confirm the presence of the Ni–O bond. However, the peak at 531.90 eV corresponds to the oxygen from water absorbed by NiO surface or shoulder peak of 1s oxygen in NiO and the peaks at 533.31 eV may be attributed due to the formation of C–O–Ni linkage in NiO (Zhou et al., 2012; Y. Zhang et al., 2016).

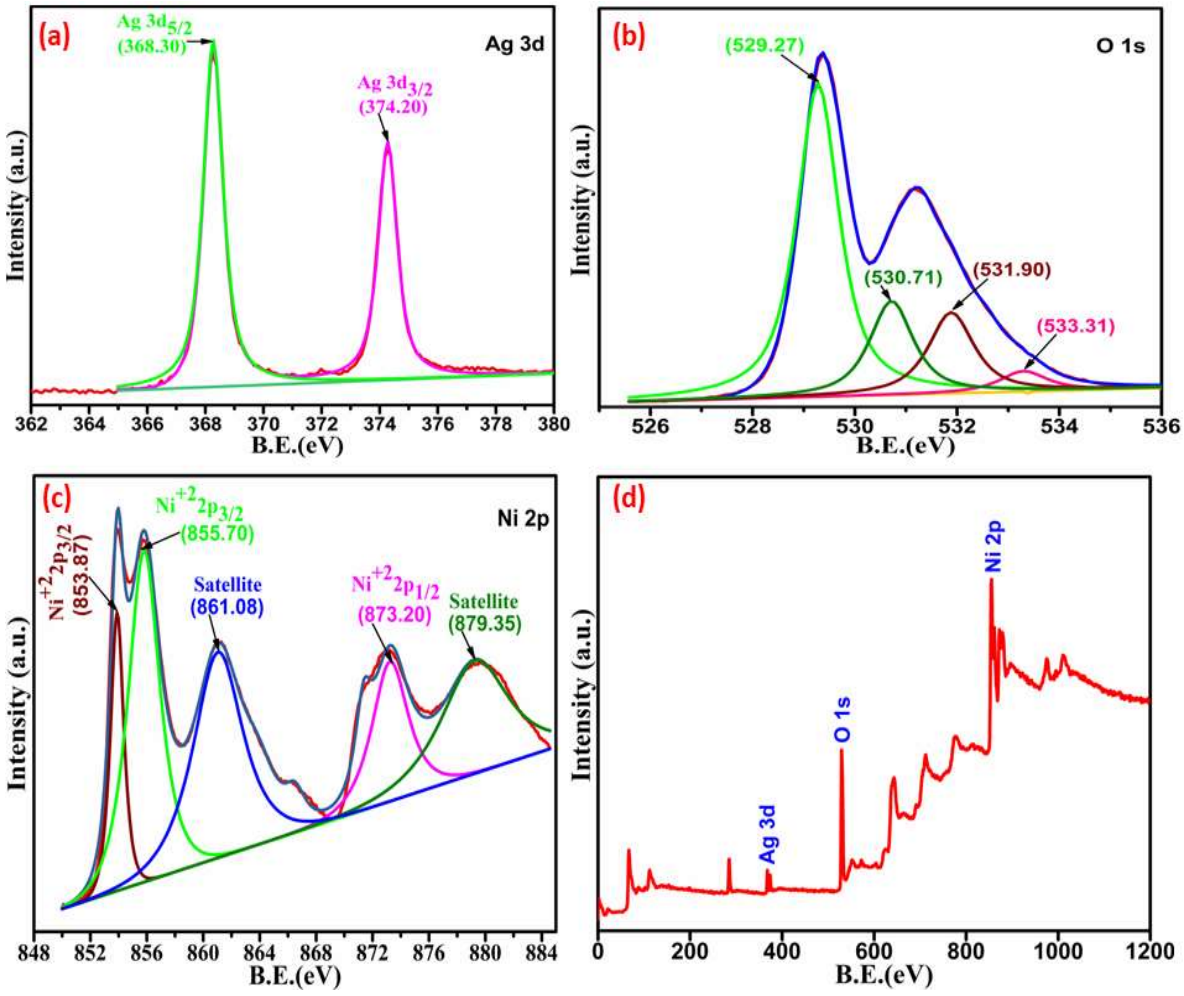

Fig. 4.6 XPS spectrum of (a) Silver, (b) Oxygen, (c) Nickel, and (d) XPS survey of LT-2.

(Note: labeled peaks in figure a-c were obtained from XPS PEAK 41 software)

Figure 4.6c contains a peak at 853.87 eV is mainly due to the Ni in $2p_{3/2}$ and the peak at 873.20 eV corresponds to Ni $2p_{1/2}$ state, which indicates the existence of Ni in +2 chemical state (Y. Zhang et al., 2016); whereas the other peaks at 861.08 and 879.35 eV are the satellite peak that comes into account by shake-up (Dai et al., 2014). The existence of Ni_2O_3 is also confirmed by the appearance of the peak of Ni ($2p_{3/2}$) at 855.70 eV and the peak of O (1s) at 533.31eV (Kim and Davis, 1972). From the above results, we observed a slight variation of the binding energies correspond to Ag 3d, Ni 2p, and O 1s; this is happening because of the transfer of the electron and interfacial interaction, which creates inequality into the electronic concentrations (Manders et al., 2013; Dupin et al., 2000; Kim et al., 2013). Figure 4.6d represents the XPS survey, which validates the presence of all the elements discussed above.

4.4.5 B.E.T.

For analysis of the textural property, the samples were characterized through N_2 adsorption-desorption isotherm and the results corresponding to L-1 and LT-2 samples are shown in figure 4.7a and b respectively. It can be seen from the figure that, both L-1 and LT-2 displays a typical H3 type hysteresis loop which indicates the mesoporous nature of the samples. The pore diameter of the samples was obtained from BJH model and it was found to be 45-50 nm, for L-1 and LT-2 samples, inset of figure 4.7a and b. There are various existing parameters which influence activity of the photocatalyst, and the surface area is one of them.

The BET equation was applied to calculate the specific surface area of the sample and the calculated surface area of LT-2 is 20 m^2/g which is higher than L-1 13 m^2/g; Thus, the higher surface area of LT-2 nanocomposite provides space for the adsorption of more number of dye (organic reactant) molecules on the surface of the catalyst, which could enhance the

photocatalytic activity.

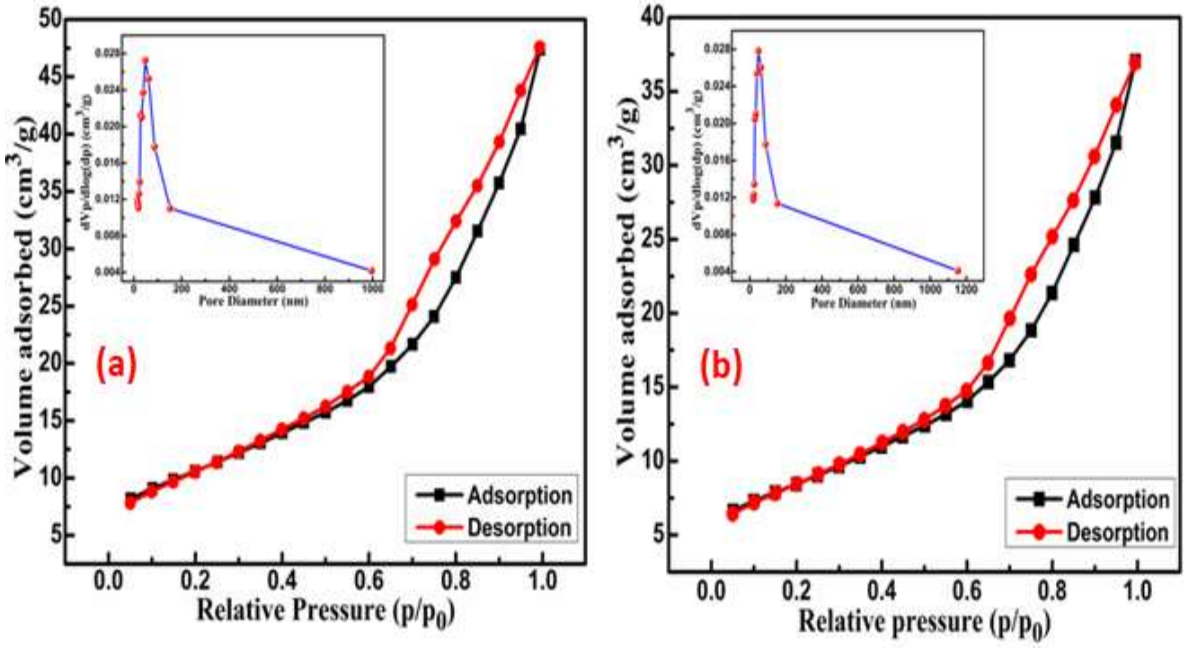

Fig. 4.7 Nitrogen adsorption-desorption isotherm and BJH pore size distribution (inset) of (a) L-1 (b) LT-2

4.5 Optical property analysis

The investigation of bandgap energy in the desired range is necessary for the photocatalytic processe. After knowing the bandgap of the materials, the estimation of the appropriate mechanism is quite simple. Thus for bandgap calculation, we measured the absorbance data from UV–Vis. DRS. The bandgap of the photocatalyst L-1, LT-1, LT-2, and LT-3 was calculated by using the Tauc relation (refer equation 3.2).

The plot of $(\alpha h\nu)^2$ versus $h\nu$ gives the bandgap energy of materials, which is given in figure 4.8a. The calculated, band gaps of L-1, LT-1, LT-2, and LT-3 nanocomposite are 3.22, 3.01, 2.82, and 2.93 eV, respectively.

4.5.1 Photoluminescence spectra

Photoluminescence (PL) spectrum plays a vital role in the elucidation of the charge transfer

and recombination of the photogenerated excitons. As we know, lower PL intensity delayed the process of charge recombination which is responsible for better photocatalytic activity (Wang et al., 2014; Kumar et al., 2017; Fujihara et al., 2000). The result of the PL spectrum of the samples L-1, LT-1, LT-2 and LT-3 is displayed in figure 4.8b. The excitation wavelength for all the samples was 254 nm. It can be seen from the figure (4.8b) that, Ag/NiO nanocomposites have lower PL intensities than pure NiO. Moreover, PL intensity of LT-2 is lowest which helps in the improvement of the charge separation and has highest photocatalytic efficiency. However on increasing the amount of Ag in LT-2 to LT-3, we get increment in the PL intensity which may be due to the aggregation of the Ag over the NiO surface and it may behave as a charge recombination centre in the nanocomposite (Li and Wang, 2011).

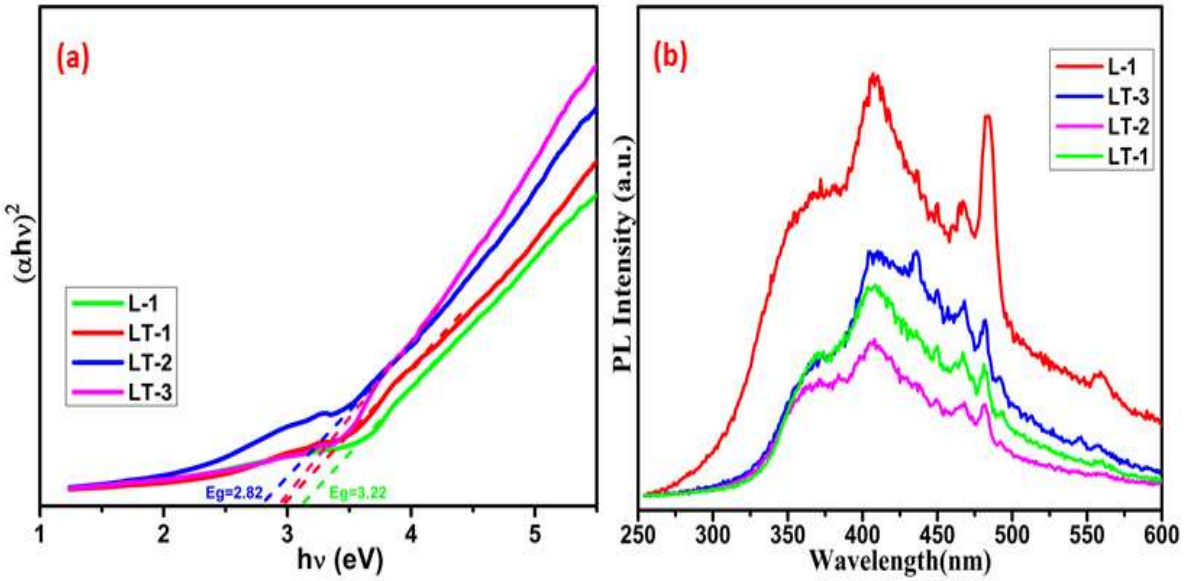

Fig. 4.8 (a) Tauc plot of L-1, LT-1, LT-2 and LT-3 samples (b) Photoluminescence spectra of L-1, LT-1, LT-2 and LT-3.

4.5.2 Photocatalytic degradation measurements

The performance of the synthesized photocatalysts was evaluated by the mineralization of

RhB dye under UV light. The characteristic absorbance peak of RhB observed at 554 nm was used as the signature during the entire process, and no new additional peaks appeared in the photocatalytic experiment. As figure 4.9b represents photocatalytic degradation of RhB with LT-2, which shows that the characteristic peak of the dye is almost vanished (97%) after 100 min interval, and no substantive change was observed beyond 100 min. So this time was taken as the standard for all the experiments.

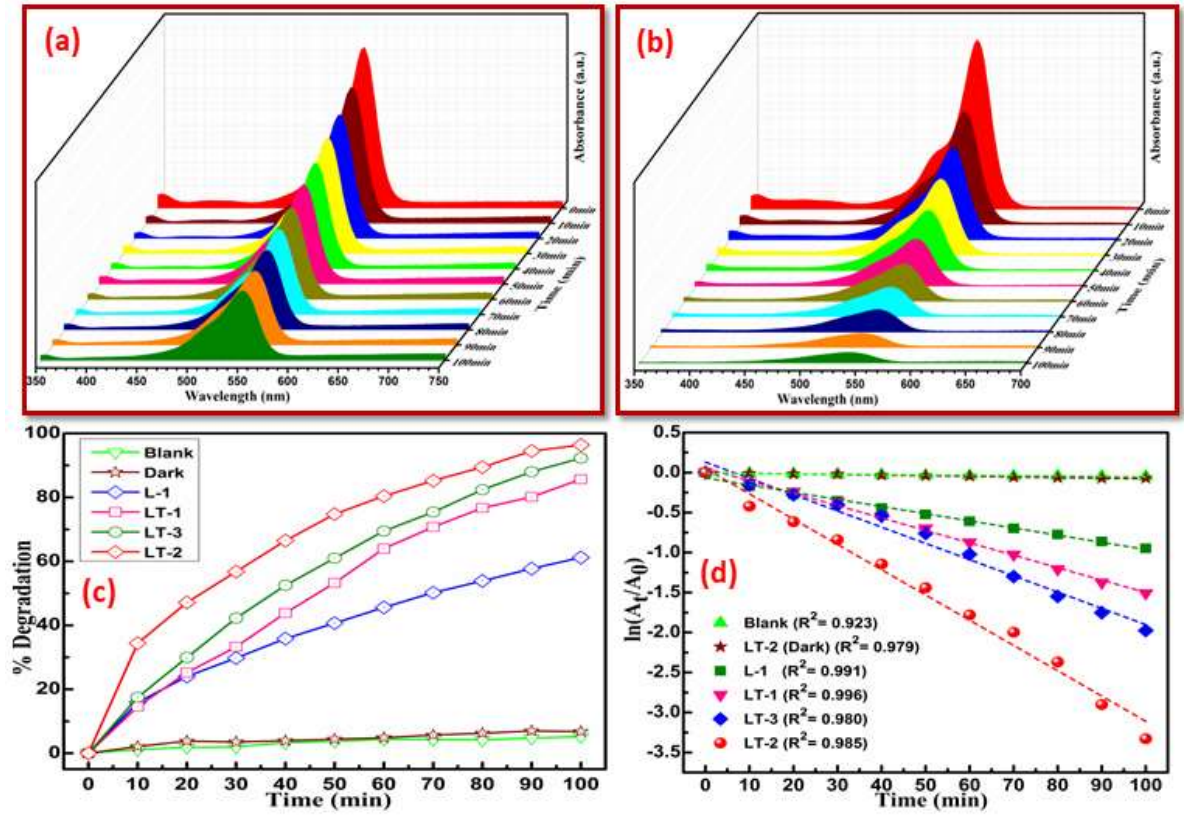

Fig. 4.9 (a, b) UV-Vis absorbance spectra of RhB with L-1and LT-2 respectively (c) percentage degradation plot (d) kinetic plot of L-1, LT-1, LT-2 and LT-3

Figure 4.9a displays that L-1 degrades only 61% of the RhB dye in the same time period while figure 4.10c shows the absorbance spectrum of RhB degradation by T-1 which was found to be 25% after 100 min. However, no significant change in the absorbance was observed for blank RhB (without catalyst), and only 7% dye was adsorbed on the surface of

LT-2 under dark conditions (figure 4.10a and b). Furthermore, percentage degradation of the dye with different samples is presented in figure 4.9c, which depicts that LT-2 mineralizes the highest percentage of RhB among all the other samples because of the creation of a robust interface between Ag and NiO, narrow bandgap, and restrained recombination of photo-generated charge carriers. Equation (3.3) was used to find out the rate constant and the order of the reaction.

Figure 4.9d displays the plot of $\ln\left(\frac{A_0}{A_t}\right)$ versus t for L-1, LT-1, LT-2, and LT-3 catalyst. The rate constant of photocatalysts obtained from slopes of the plot is given in Table 4.1 reveals that LT-2 has the highest value of the rate constant. Linear fitting of kinetic plots demonstrates that photocatalytic degradation of RhB with the catalyst is of pseudo 1st order.

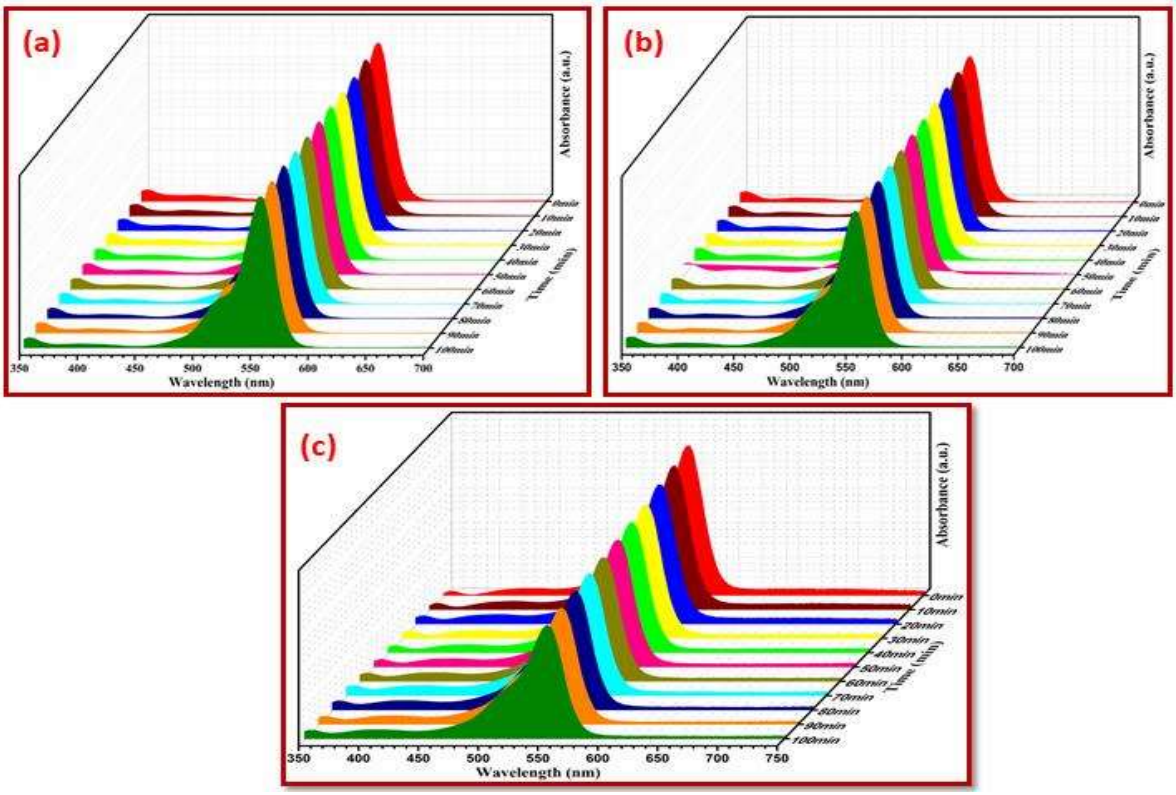

Fig. 4.10 UV-Visible absorbance spectra of RhB degradation (a) Blank (b) With LT-2 in dark (c) With T-1

Table 4.1 Comparison of kinetic parameters (R^2 and rate constant) and % degradation

Sample	Linear Coefficient (R^2)	Rate constant (min^{-1})	Degradation (%)	Irradiation time (min)	
Ag/NiO	0.954	8.0×10^{-3}	75	200	(Ghazal et al., 2020)
L-1	0.991	8.95×10^{-3}	61	100	This work
LT-1	0.996	1.55×10^{-2}	85	100	This work
LT-2	***0.985***	***3.16×10^{-2}***	***97***	***100***	***This work***
LT-3	0.970	2.43×10^{-2}	92	100	This work

4.5.3 Effect of loading of silver

Figure 4.9c displays the effect of silver loading over NiO. As, we can see that the photocatalytic degradation of RhB dye with porous NiO (L-1) and T-1 is minimum as compared to modified NiO, i.e., Ag/NiO (LT-1, LT-2, LT-3) nanocomposite photocatalyst, which is due to a wide bandgap of NiO and fast recombination rate of charge carriers, while Ag/NiO displays higher photocatalytic degradation efficiency as expected because of the suppressed rate of recombination. The photocatalytic efficiency of Ag/NiO increases with increasing amount of Ag in LT-1 to LT-2, but after an optimum amount of Ag in LT-2, further increment in the atomic percentage of Ag causes suppression in the photocatalytic activity. Thus, LT-2 displays the highest photocatalytic performance towards the degradation of RhB, and this happens because of better interfacial contact in between Ag and porous NiO, whereas the increment in the content of Ag after an optimum amount suppresses the

photocatalytic activity due to the hindered path of light resulting very small percentage of the light reaching the interface of the photocatalyst.

4.5.4 Observation of active species involved in dye degradation

In order to investigate the chief reactive species generated during the mineralization process of RhB, various trapping agents like p-benzoquinone (PBQ), iso-propyl alcohol (IPA), and potassium iodide (KI) were employed to extinguish the role of $O_2^{\bullet-}$ radicals, $OH^{\bullet}$ radicals, and holes (h^+) respectively; the same concentration (2×10^{-3} M) of the scavengers was added in distinct photocatalytic degradation experiments to find out the effect of these scavengers on the photocatalytic efficiency of LT-2.

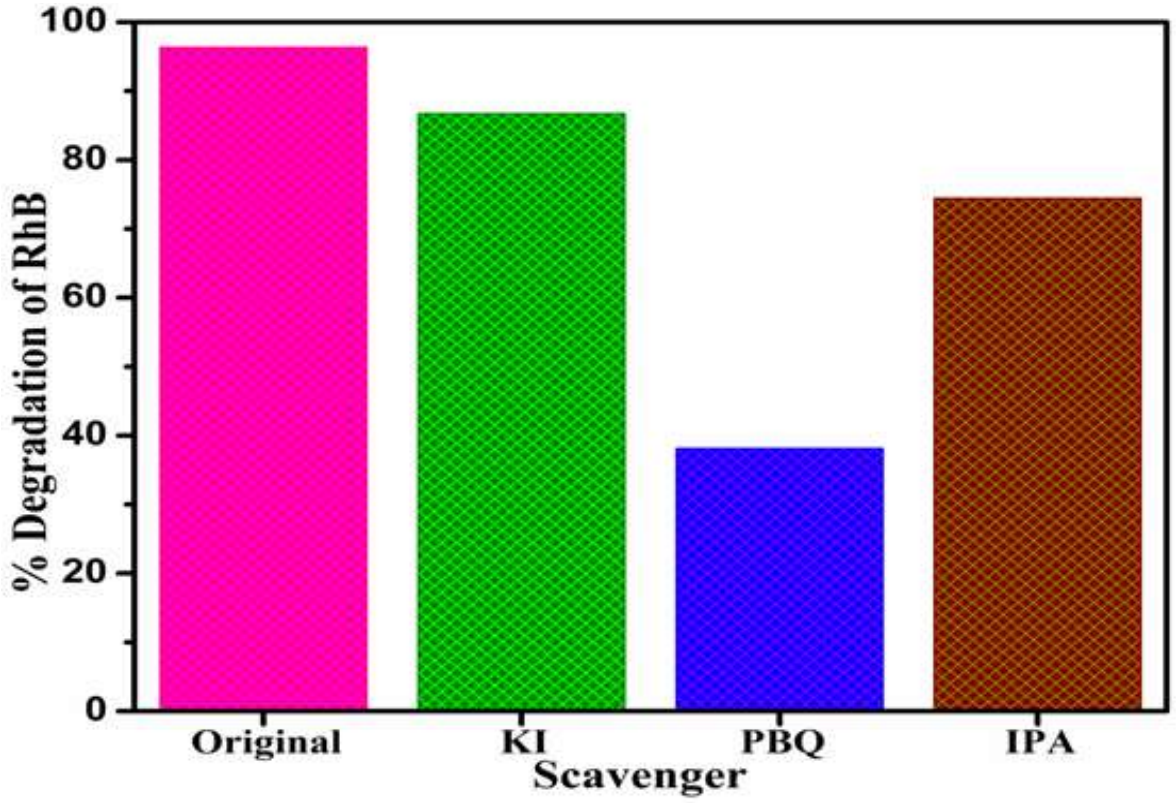

Fig. 4.11 Result of trapping experiments

This study was done only with LT-2, as initially the photocatalytic efficiency of this photocatalyst was found highest. The result of trapping experiment is displayed in figure 4.11

which depicts that there is only a minimal decrease in photodegradation efficiency of RhB over LT-2 photocatalyst with KI and IPA, which depict that the holes and $OH^{\bullet}$ radicals are not the primary reactive species generated during the photocatalytic process. In contrast to this, the degradation efficiency of LT-2 is greatly decreased with the addition of PBQ. These results suggest that although all the three active species were formed during the degradation experiment but $O_2^{\bullet-}$ radical plays a significant role in photocatalytic mineralization of RhB dye.

4.6 Mechanism of photocatalytic degradation

Our primary motive behind using noble metal as a dopant is to tune or reform the band position as well as photocatalytic properties of the semiconductor. Incorporation of silver into metal oxide nanoparticles modifies the bandgap of the semiconductor. Figure 4.12 depicts the plausible mechanism of the photocatalytic degradation where the formation of the interface between Ag and NiO is posited. When the photocatalyst (Ag/NiO) was irradiated by UV light, the electrons transit from valence band (VB) to conduction band (CB) of NiO, and this photogenerated electron in the CB of NiO is further taken by Ag, which reduces the oxygen from the atmosphere and produces the anionic superoxide ($O_2^{\bullet-}$) radical, in the meantime the holes created in the VB of NiO reacts with surface water and oxidize it into hydroxyl ($OH^{\bullet}$) radical. Further, these reactive radical intermediates react with aqueous RhB dye solution and mineralize into colorless species (CO_2 and H_2O). So, the Ag/NiO photocatalyst provides an interface and large surface area to produce oxygen vacancies and the plasmonic effect of silver itself enables Ag/NiO nanocomposites as a dominant photocatalyst than pure NiO.

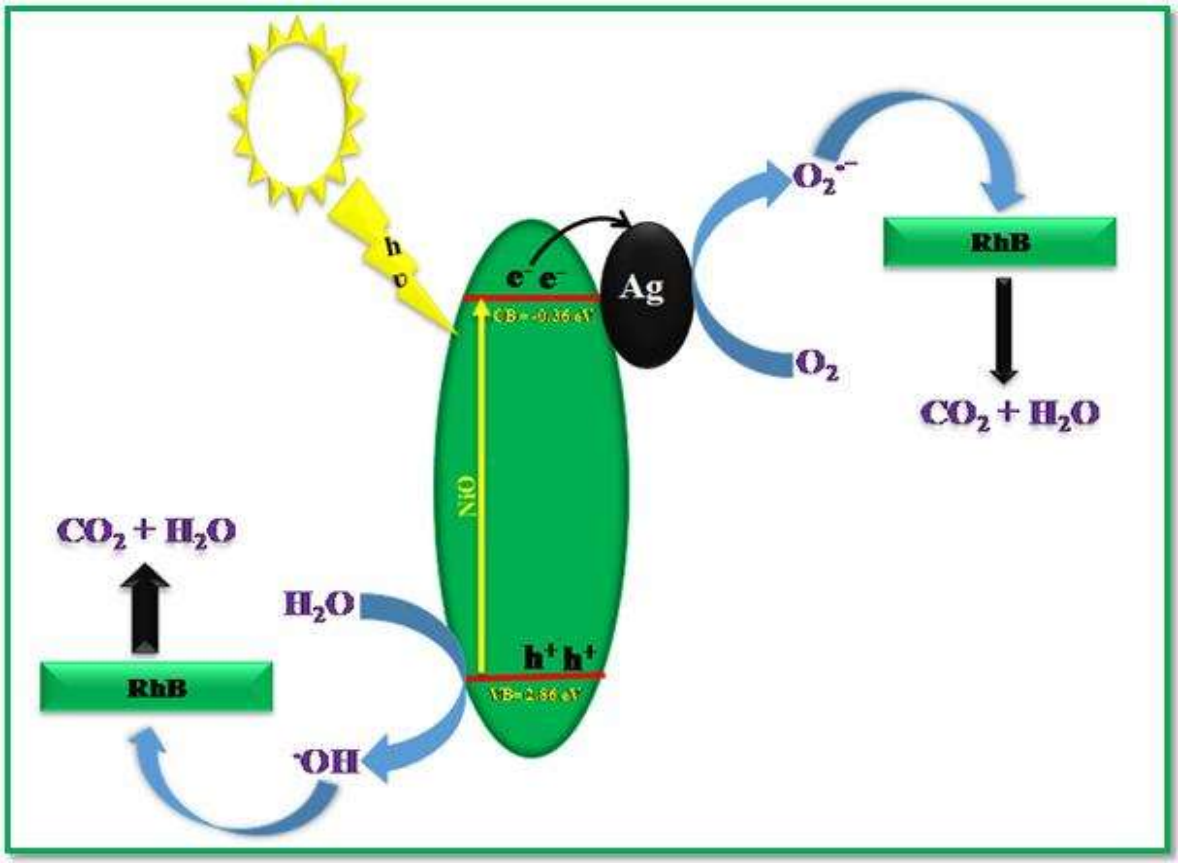

Fig. 4.12 Plausible photocatalytic mechanism for LT-2

4.6.1 Turnover frequency (TOF) of photocatalyst

TOF is a good indicator for knowing the efficiency of a catalyst (Prakash et al., 2015; Pandey et al., 2021). The TOF of the LT-2 photocatalysts was calculated by using equation (3.6). Table 4.2 compares the TOF of various investigations on the degradation of RhB and other pollutants. It can be seen from the table 4.2 that our catalyst has highest TOF value than previously published articles (using UV light source). Moreover, the turnover number (TON) of the LT-2 nanocomposite is also found highest (refer table 4.2). The TON was calculated by using following formula:

$$\boldsymbol{Turn\ Over\ Number\ (TON) = TOF\ \times time\ (min.)} \qquad \boldsymbol{(4.1)}$$

Table 4.2 Comparison table of TOF of present investigation with previous works

S. No.	Photocatalysts	Irradiation Source	TOF [mole $g^{-1}min^{-1}$]	TON [mole g^{-1}]	Reference
1	Chitosan/SnO_2	UV light (8W)	3.95×10^{-7}	3.95×10^{-5}	(Gupta et al., 2017)
2.	ZnO	UV lamp (400W)	3.49×10^{-7}	2.44×10^{-5}	(Nandi and Das, 2019)
3.	Eu/ZnO	UV light (100W)	1.61×10^{-7}	2.89×10^{-5}	(Zong et al., 2014)
4.	Fe_3O_4@SiO_2@ZnO–Ag	Mercury lamp (250W)	1.62×10^{-7}	1.45×10^{-5}	(Wang et al., 2015)
5.	Chitosan/CdO/NiO	Mercury lamp (8W)	1.75×10^{-7}	1.57×10^{-5}	(Linda et al., 2016)
6.	NiO/$AgNbO_3$	Mercury lamp (125 W)	1.47×10^{-7}	2.64×10^{-5}	(Shu et al., 2010, p. 3)
7.	Se-ZnS	Mercury lamp (125 W)	5.96×10^{-8}	9.53×10^{-6}	(Ahluwalia et al., 2016)
8.	***Ag-NiO (LT-2)***	***UV light (8W)***	$\boldsymbol{2.02\times10^{-6}}$	$\boldsymbol{2.02\times10^{-4}}$	***This work***

4.7 Recyclability experiment

The photocatalytic stability of the most efficient LT-2 photocatalyst was investigated by a reusability experiment. After each cyclic experiment, the photocatalyst was collected and washed with water, followed by drying at 100 °C and afterward utilized for the next cycle. For each recyclability experiment, the reaction duration is fixed, 100 min. The results of recyclability are displayed in figure 4.13a, which reveals that the mineralization efficiency of

the photocatalyst remains unchanged till 3rd cycle, and after that, only a slight decrement was observed, which validates the stability of the photocatalyst. This examination was further confirmed by characterizing the used catalyst through XRD techniques that have good agreement with the XRD pattern of the fresh catalyst without any photo corrosion and the peaks are matched with the JCPDS card no. 87–0719 and 47–1049. The XRD result of the used catalyst is given in figure 4.13b.

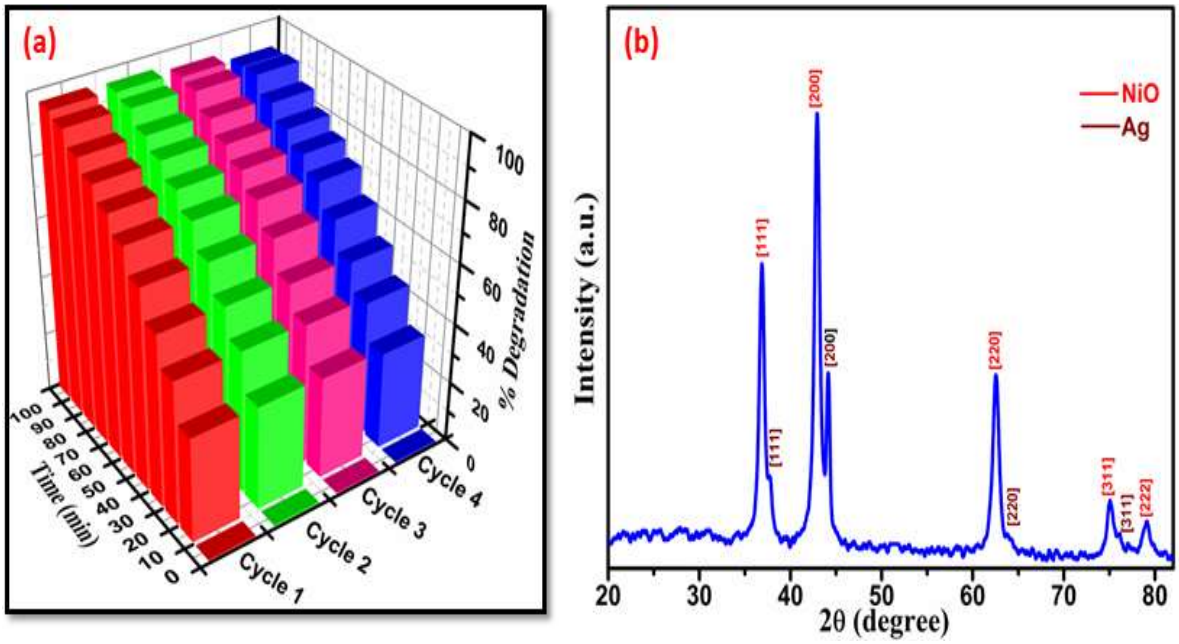

Fig. 4.13 (a) Recyclability of LT-2 (b) XRD pattern of LT-2 after recyclability

4.8 Summary and conclusion

Based on the above results and discussion, we conclude our work as follows:–

- The activity of the Ag/NiO nanocomposites synthesized by the sol-gel method was studied for the mineralization of organic dye under UV light illumination.
- Size of the heterostructure is in the range of the 15–20 nm that was well supported by the XRD prediction (i.e., crystallite size).

- The positive effect of Ag was observed on the photocatalytic performance of NiO, which is due to the restrained recombination rate as silver traps the photogenerated electrons.
- A close interfacial contact between Ag and NiO as well as the high surface area provides space to create large oxygen vacancies which facilitate the photocatalytic activity of the nanocomposites.
- Superoxide radical ($O_2^{\bullet-}$) is the primary intermediate that is responsible for the mineralization of the RhB.
- Photocatalyst LT-2 shows the highest mineralization capacity along with a higher rate constant value (3.16×10^{-2} min^{-1}), which is upto 97% in 100 min.
- TOF value of the LT-2 (**2.02×10^{-6} mole $g^{-1}min^{-1}$**) is higher than the TOF of cited literature in Table 4.2.
- Recyclability experiment confirms the efficiency and stability of LT-2 catalyst with negligible photocorrosion.